Available online at www.sciencedirect.com
ScienceDirect
Journal of Power Sources 161 (2006) 380–391
JOURNAL OF POWER SOURCES
www.elsevier.com/locate/jpowsour

Effects of transport scale on heat/mass transfer and performance optimization for solid oxide fuel cells

Yan Ji [a], Kun Yuan [a], J.N. Chung [a,*], Yen-Cho Chen [b]

[a] *Department of Mechanical and Aerospace Engineering, University of Florida, FL 32611-6300, USA*
[b] *Department of Energy and Resources, National United University, Miao-Li, Taiwan, ROC*

Received 16 February 2006; received in revised form 7 April 2006; accepted 10 April 2006
Available online 15 June 2006

Abstract

A three-dimensional thermo-fluid–electrochemical model is developed to study the heat/mass transport process and performance of a solid oxide fuel cell (SOFC). The main objectives are to examine the transport channel size effects and to assess the potential of a thin-film-SOFC. A parametric study was performed to evaluate the channel scale effects on the temperature, species concentration, local current density and power density. The results demonstrate that decreasing the height of flow channels can lower the average solid temperature and improve cell efficiency. However, this improvement is rather limited for the smallest channels. Compared with the conventionally sized SOFC, the miniaturized SOFC with a thin-film electrolyte has the advantages of a lower operating temperature and a better performance. Based on our simulation results, the power density of a miniaturized SOFC could reach up to 5.461 W cm^{-3}. However, an extremely small structure will lead to severe thermal stress induced by a large temperature gradient, a cell with a thicker rib width would have a higher efficiency and a lower average temperature. Numerical simulation is expected to help optimize the design of a solid oxide fuel cell.
© 2006 Elsevier B.V. All rights reserved.

Keywords: Solid oxide fuel cell; Geometry scale; Heat/mass transfer; Optimization; Modeling

1. Introduction

Solid oxide fuel cells are expected to be widely applicable for both small and large-scale power generation systems. The reason is that the solid oxide fuel cell (SOFC) is simple, highly efficient, tolerant of impurities, and can at least partially reform hydrocarbon fuels internally. However, the application of a SOFC is bounded by some limitations, which are primarily due to its high operating temperature (1000–1200 °C), expensive materials, difficulties in fabrication, large thermal stresses within the cells, etc. [1,2]. Major efforts have been placed on the materials, designs of a novel geometry, and improvement in power density along with lowering the operating temperature down to 500–700 °C [3–10]. Ramakrishna et al. [4] developed a new type of SOFC, which has a thin-wall geometry. Because of a better longitudinal reactant distribution along the thin-wall geometry, they were able to improve the SOFC performance and achieve a maximum power density of 1.18 W cm^{-2}. Recently, Hwang et al. [6] have performed computational studies on a MOLB (monoblock-layer-built)-type SOFC. In their study, it is reported that the MOLB-type SOFC has a higher fuel/oxidant utilization ratio than a planar SOFC. Similar computational studies have also been carried out by Lu and Schaefer for flat tube HPD-SOFC [7].

In order to minimize the overall losses, alleviate the thermal stress and improve the electrolyte-supported SOFC efficiency, key parameters governing the polarizations and heat/mass transfer efficiency should be investigated. Basically, for a given operating condition, there are three kinds of mechanisms that cause the overall losses [1]: (1) ohmic polarization, which is from the ohmic resistances of all components and contact interfaces; (2) activation polarizations at the anode and cathode, which are related to charge transfer processes and depend on the nature of electrode–electrolyte interfaces; (3) concentration polarization, which is associated with the transport of gas species and thus depends on the channel dimensions, electrode geometry, and the nature of electrode microstructure, i.e. porosity and tortuosity. For an electrolyte-supported SOFC, a larger ohmic polariza-

* Corresponding author. Tel.: +1 352 392 9607; fax: +1 352 392 1071.
E-mail address: jnchung@ufl.edu (J.N. Chung).

0378-7753/$ – see front matter © 2006 Elsevier B.V. All rights reserved.
doi:10.1016/j.jpowsour.2006.04.097

Nomenclature

A_{area}	active area (m^2)
c	specific heat capacity ($J\,kg^{-1}\,K^{-1}$)
C_i	molar concentration of component i ($mol\,m^{-3}$)
D_{ij}	binary mass diffusivity ($m^2\,s^{-1}$)
$D_{i,k}$	effective Knudsen diffusion coefficient for component i ($m^2\,s^{-1}$)
E	Nernst potential (V)
F	Faraday's constant, 96486.7 ($C\,mol^{-1}$)
F_1	Forchheimer coefficient
ΔG	chemical potential ($J\,mol^{-1}$)
h	heat transfer coefficient ($W\,m^{-2}\,K^{-1}$)
$h_{m,i}$	mass transfer coefficient of component i ($m\,s^{-1}$)
H	channel height (m)
ΔH_{reform}, ΔH_{shift}, ΔH_{elec}	enthalpy change of reactions ($J\,mol^{-1}$)
i	local current denstiy ($A\,m^{-2}$)
i_{oa}, i_{oc}	exchange current density of anode or cathode ($A\,m^{-2}$)
L	channel length (m)
$\vec{J}$	diffusion mass flux vector
k	thermal conductivity ($W\,m^{-1}\,K^{-1}$)
k_r^+, k_r^-, k_{sh}^+, k_{sh}^-	velocity constants for reforming or shift reaciton
K	permeability of the porous medium (m^2)
m_i''	molar consumption or production rate of component i at the electrode/electrolyte interface ($mol\,m^{-2}\,s^{-1}$)
M_i	molar weight of component i ($kg\,mol^{-1}$)
n_e	number of electron
p_i	partial pressure of component i (atm)
$p_{O_2}^r$	partial pressure of oxygen at reaction site (atm)
P	pressure (Pa)
q''	heat flux at interface ($W\,m^{-2}$)
q''_{elec}	heat flux from electrochemical reaction ($W\,m^{-2}$)
Q_{oh}, Q_{re}	volumetric heat generation ($W\,m^{-3}$)
$\bar{r}$	aveage pore radius (m)
R_{ax}, R_{az}, R_{cx}, R_{cz}, R_e, R_{inb}, R_{int}	resistance of electrodes, electrolyte and interconnectors (Ω)
R_g	universal gas constant, 8.3143 ($J\,mol^{-1}\,K^{-1}$)
$R_{r,i}$, $R_{sh,i}$	volumetric reaction rates of component i in reforming or shift reaction ($mol\,m^{-3}\,s^{-1}$)
S_i	net rate of production for component i
T	temperature (K)
$\vec{V}$	velocity vector ($m\,s^{-1}$)
X_i	molar fraction of component i
Y_i	mass fraction of component i

Greek letters

β	transfer coefficient
ε	porosity
$\eta_{act,an}$, $\eta_{act,ca}$	activation overpotential (V)
η_{con}	concentration overpotential (V)
μ	viscosity ($m^2\,s^{-1}$)
ν_{int}	interface velocity ($m\,s^{-1}$)
φ	ratio of porosity to tortuosity
ρ	density ($kg\,m^{-3}$)
σ	electrical conductivity ($\Omega^{-1}\,m^{-1}$)
ϕ	electrical potential (V)

Subscripts

an	anode
b	bulk
ca	cathode
eff	effective
f	flow
i	components in gas mixture (fuel channel mixture: $i = CH_4$, CO, CO_2, H_2, H_2O; air channel mixture: $i = O_2$, N_2)
int	interface
s	solid

tion in the electrolyte is a serious problem, so developing a thin-film electrolyte to substantially reduce the ohmic loss is a worthwhile approach [8–10]. In general, with the dimension of flow channel decreasing from conventional to microscale dimensions, the temperature/concentration gradient decreases and the heat/mass transfer coefficient increases. Moreover, minimized sizes are important to developing low cost and portable SOFCs. One therefore expects that concentration loss and operating temperature in smaller fuel cells would be effectively reduced.

However, only a few investigations address the issues of thermal stress, the heat/mass transfer efficiency and cell performance for flow channels whose characteristic dimension is less than 1.0 mm [10–12]. On the other hand, a small scale may lead to thermal management difficulties and poor thermal cyclability, etc. Recently, Li et al. [11] proposed a new design for the fuel cell gas distributor by maximizing the access area of reactants for enhancing mass transfer, and were able to increase the maximum output power by 40% for a single cell. These potential advantages motivate us to investigate the scaling effects, especially of miniaturized flow channels, on the performance of a SOFC. Other geometrical parameters, such as the rib width and electrolyte thickness, also have strong effects on the performance of a fuel cell and should be optimized.

Considering the complexity of the actual energy transport process in SOFCs, a mathematical model is usually a desirable tool to analyze the phenomena inside a SOFC and predict its performance. Over the past decades, various models have been proposed based on different complexity levels, ranging from the molecular-level via the cell component-level, and the cell-level to the system-level [6,7,13–20]. In the present study, a 3D thermo-fluid–electrochemical model was developed to simulate the heat/mass transport and electrochemical process. The geometry of the interconnector (or rib) and microstructures of electrodes were considered. Based on this model, the effects of channel height, thin-film electrolyte, and rib thickness on the performance characteristics of a SOFC were quantitatively investigated and the following issues were addressed: (1) To

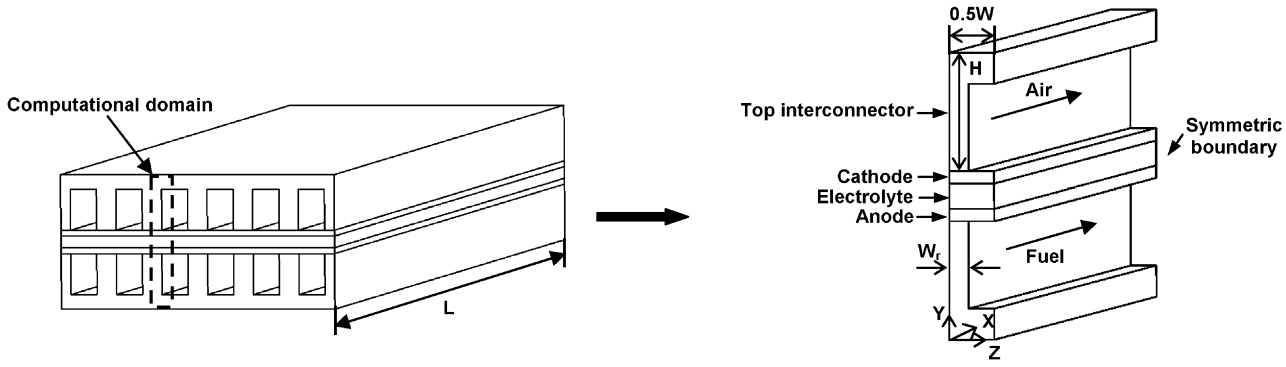

Fig. 1. Schematic of a co-flow planar SOFC and the computational domain.

what extent does the channel dimension affect the heat/mass transfer? (2) As the height of a flow channel is decreased, whether or not the power density is improved and the solid temperature rise is suppressed? (3) Whether or not the thin-film electrolyte improves the performance of a SOFC? (4) What is the optimal thickness of the rib? (5) How do the above variations in geometry affect the thermal stress?

2. Description of modeling

The stack of a SOFC is made up of many identical unit cells connected in parallel, most of which function under similar operation conditions. Therefore, to reduce computational work, only one unit cell is taken as the computational domain. This typical single cell is assumed to be an interior and non-boundary unit. As a result, the heat loss to the surroundings is not considered and the only heat removal mechanism from the cell is through the gas streams. The schematic of the computational model is shown in Fig. 1. Furthermore, only one half of the gas channels are modeled by applying the symmetry condition. A single cell consists of a porous layer of anode, a porous layer of cathode, a dense layer of electrolyte, and interconnectors (or ribs). The interconnectors support the structure and also serve as the current collectors. When air and fuel streams flow along the *X*-direction (co-flow arrangement), O_2 gas from the air stream diffuses through the cathode and accepts electrons from the external circuit at the cathode/electrolyte interface. Also, at the anode/electrolyte interface the oxygen ions pass through the electrolyte and react with the H_2, and the reaction product H_2O diffuses back into the fuel stream. If the fuel is natural gas (CH_4, CO_2, CO, H_2, and H_2O), the reforming and shift reactions take place through the anode layer as follows:

Reforming : $CH_4 + H_2O \leftrightarrow 3H_2 + CO + 206\,\text{kJ/mol}$

Water-gas shift : $CO + H_2O \leftrightarrow H_2 + CO_2 - 41\,\text{kJ/mol}.$

There are several assumptions that should be pointed out in the present model: (1) transport and gradients in all three-directions are considered; (2) energy transfer due to species diffusion in channel flows and porous layers are neglected; (3) because the single cell model represents a repeating cell unit in the center of a larger stack, cyclic boundary conditions for current are imposed at the boundaries of model domain. Walls at the periphery of the single cell are assumed to be adiabatic.

2.1. Thermal-fluid model

In this model, the entire computational domain consists of three sub-domains: porous (electrodes), solid (interconnectors and electrolyte) and pure fluid regions (channel flows). It has been demonstrated by previous experiments that the fluid flow in the porous media is a low speed mixed gas flow with a Reynolds number much less than unity. Therefore, this flow is treated as laminar and incompressible. It is also assumed that the porous medium is homogeneous and in local thermodynamic equilibrium with the fluid. In the porous region, the flow is governed by the Brinkman-Forchheimer extended Darcy model, which takes into account the effects of flow inertia as well as friction induced by macroscopic shear stresses. While in the fluid region, the Navier-Stokes equations describe the flow behavior. The conservation equations of mass, momentum, energy and species for fluids in both pure fluid region and porous domain are:

$$\nabla \cdot (\rho_f \vec{V}) = 0 \tag{1}$$

$$\frac{\rho_f}{\varepsilon}\nabla \cdot (\vec{V}\vec{V}) = -\frac{\nabla P}{\varepsilon} + \frac{\mu_f}{\varepsilon}\nabla^2 \vec{V} - \chi\left(\frac{\mu_f}{K}\vec{V} + \frac{\rho_f F_1 \varepsilon}{\sqrt{K}}\left|\vec{V}\right| \cdot \vec{V}\right) \tag{2}$$

$$\nabla \cdot (\varepsilon \rho_f c_f \vec{V} T) = \nabla \cdot (k_{\text{eff}} \nabla T) + Q_{\text{re}} + Q_{\text{oh}} \tag{3}$$

$$\nabla \cdot (\varepsilon \rho_f Y_i \vec{V}) = -\nabla \cdot \vec{J}_i + S_i \tag{4}$$

$$\sum_{i=1}^{n} Y_i = 1 \tag{5}$$

$$\rho_f = \frac{P}{R_g T \left(\sum_i Y_i / M_i\right)} \tag{6}$$

where the parameter χ is set to unity for the flow in a porous medium ($0 < \varepsilon < 1$) and to zero in regions without a porous material ($\varepsilon = 1$). $\vec{V}$ and Y_i represent velocity vector and local mass fraction of each component, respectively. ε is the porosity and K is the permeability of the porous medium. F_1, the Forchheimer coefficient is calculated by $F_1 = 1.8/(180\varepsilon^5)^{0.5}$. The effective

thermal conductivity k_{eff} is equal to $\varepsilon k_{\text{f}} + (1-\varepsilon)k_{\text{s}}$. The heat source Q_{oh} is due to ohmic loss and activation overpotentials. Another source term, Q_{re}, denotes the heat produced by reforming and shift reactions, which only takes place in the anode layer. There is no heat generation term in pure fluid region. Thus, once the information of the electrical field and chemical reactions is obtained, the two heat source terms can be exactly determined. S_i is the net rate of production of component i by chemical reaction and is left for specific discussion later. $\vec{J}_i$ is the diffusion mass flux vector derived from the Stefan-Maxwell relation [21]:

$$\frac{\vec{J}_i}{D_{i,\text{k}}} + \sum_{\substack{i=1 \\ j \neq i}}^{n} \left(\frac{X_i \vec{J}_j}{D_{ij,\text{eff}}} - \frac{X_j \vec{J}_i}{D_{ij,\text{eff}}} \right) = \frac{P}{R_{\text{g}} T} \nabla X_i \tag{7}$$

where X_i is the mole fraction of component i and $D_{ij,\text{eff}}$ is the effective binary diffusion coefficient of a mixture of components i and j and equal to φD_{ij}. φ is the ratio of porosity to tortuosity. $D_{i,\text{k}}$ is the effective Knudsen diffusion coefficient of component i and calculated according to the kinetic theory of gas:

$$D_{i,\text{k}} = \varphi \frac{2}{3} \sqrt{\frac{8 R_{\text{g}} T}{\pi M_i}} \bar{r} \tag{8}$$

$\bar{r}$ is the average pore radius. The density, viscosity, specific heat, and thermal conductivity are functions of both temperature and mass fraction of gas mixture. In a SOFC, the shift reaction, which takes place at high temperatures, can be assumed to react very quickly and almost in equilibrium [22]. The reforming kinetics is assumed to be quasi-homogeneous. Lehnert et al. [22] reported experimental results for the forward velocity constants (k_{r}^{+}, k_{sh}^{+}) and the backward velocity constants (k_{r}^{-}, k_{sh}^{-}) for the two reactions at three different temperatures. Habeman and Young [23] have developed empirical correlations for velocity constants with Arrhenius curve fitting technique using experimental data of Lehnert et al. [22] in the temperature range, $900 < T < 1300$ K. The volumetric reaction rates of hydrogen in a shift reaction and methane in reforming reaction are calculated by:

$$R_{\text{sh,H}_2} = k_{\text{s}}^{+} (R_{\text{g}} T)^2 C_{\text{CO}} C_{\text{H}_2\text{O}} - k_{\text{s}}^{-} (R_{\text{g}} T)^2 C_{\text{CO}_2} C_{\text{H}_2} \tag{9}$$

$$R_{\text{r,CH}_4} = k_{\text{r}}^{+} (R_{\text{g}} T)^2 C_{\text{CH}_4} C_{\text{H}_2\text{O}} - k_{\text{r}}^{-} (R_{\text{g}} T)^4 C_{\text{CO}} C_{\text{H}_2}^3 \tag{10}$$

where C_i ($i = \text{CH}_4$, CO, CO_2, H_2, H_2O) is the molar concentration of component i. The net rate of production for each component, S_i, can be stated as follows:

$$S_{\text{CH}_4} = -M_{\text{CH}_4} R_{\text{r,CH}_4} \tag{11}$$

$$S_{\text{CO}} = M_{\text{CO}} R_{\text{r,CH}_4} - M_{\text{CO}} R_{\text{sh,H}_2} \tag{12}$$

$$S_{\text{H}_2\text{O}} = -M_{\text{H}_2\text{O}} R_{\text{r,CH}_4} - M_{\text{H}_2\text{O}} R_{\text{sh,H}_2} \tag{13}$$

$$S_{\text{H}_2} = 3 M_{\text{H}_2} R_{\text{r,CH}_4} + M_{\text{H}_2} R_{\text{sh,H}_2} \tag{14}$$

$$S_{\text{CO}_2} = M_{\text{CO}_2} R_{\text{sh,H}_2}. \tag{15}$$

When the molar numbers of methane and hydrogen involved in the reaction are determined, the volumetric heat generation rate due to chemical reaction in Eq. (3) is expressed by:

$$Q_{\text{re}} = \Delta H_{\text{reform}} R_{\text{r,CH}_4} + \Delta H_{\text{shift}} R_{\text{sh,H}_2} \tag{16}$$

Note that Eq. (16) is only applicable to the anode layer. In Eq. (3), the second source term includes the heat generations from ohmic loss in all solid or porous regions and activation overpotentials in electrodes:

$$Q_{\text{oh}} = I^2 R, \quad \text{for solid or electrodes} \tag{17a}$$

$$Q_{\text{oh}} = I^2 R + \eta_{\text{act}} I, \quad \text{for electrodes} \tag{17b}$$

where I is local current and R is resistance. η_{act} is activation overpotential. It is assumed that the electrochemical reaction occurs in the vicinity of the anode/electrolyte interface, and so the thermodynamic heat generation from this reaction is:

$$q''_{\text{elec}} = (\Delta H_{\text{elec}} - \Delta G) m''_{\text{H}_2} \tag{18}$$

here ΔG is the chemical potential and m''_{H_2} is the molar consumption rate of hydrogen. In the actual calculation, Eq. (18) is treated as a heat flux condition at the anode/electrolyte interface.

2.2. Electrochemical model

The electrochemical model predicts the local electrical potential and current density, which is subject to changes in geometry, local temperature and gas compositions. Numerical simulation for a three-dimensional electrical field is directly analogous to the calculation of heat transfer using a finite volume method. A separate anode/electrolyte/cathode unit is modeled and the discretization of equivalent electric circuit is shown in Fig. 2. Within an electrolyte layer, the current primarily flows from the anode to the cathode. Electrostatic potential within all computational elements must satisfy the Laplace equation:

$$\nabla \cdot (\sigma \nabla \phi) = 0 \tag{19}$$

where σ is the electrical conductivity and ϕ is the electrical potential. The calculation of an electric field potential combines the following contributions: (1) ohmic losses in all the conducting materials, including the electrolyte, the electrodes, and the current collectors, (2) the contact resistance at interfaces and interconnector resistance, (3) activation overpotentials η_{act}, which is described by the well-known Butler-Volmer expression, in the anode and cathode layers [16]:

$$i = i_0 \left\{ \exp\left(\frac{\beta n_{\text{e}} F \eta_{\text{act}}}{R_{\text{g}} T} \right) - \exp\left[-(1-\beta) \left(\frac{n_{\text{e}} F \eta_{\text{act}}}{R_{\text{g}} T} \right) \right] \right\} \tag{20}$$

where F is the Faraday's constant. n_{e} is the number of electrons. β is the transfer coefficient. i_0 is the exchange current density. These parameters are given in Table 1. If β is chosen as 0.5, activation overpotential for the anode and the cathode can be written as follows:

$$\eta_{\text{act,an}} = \frac{R_{\text{g}} T}{F} \sinh^{-1}\left(\frac{i}{2 i_{0\text{a}}} \right) \tag{21}$$

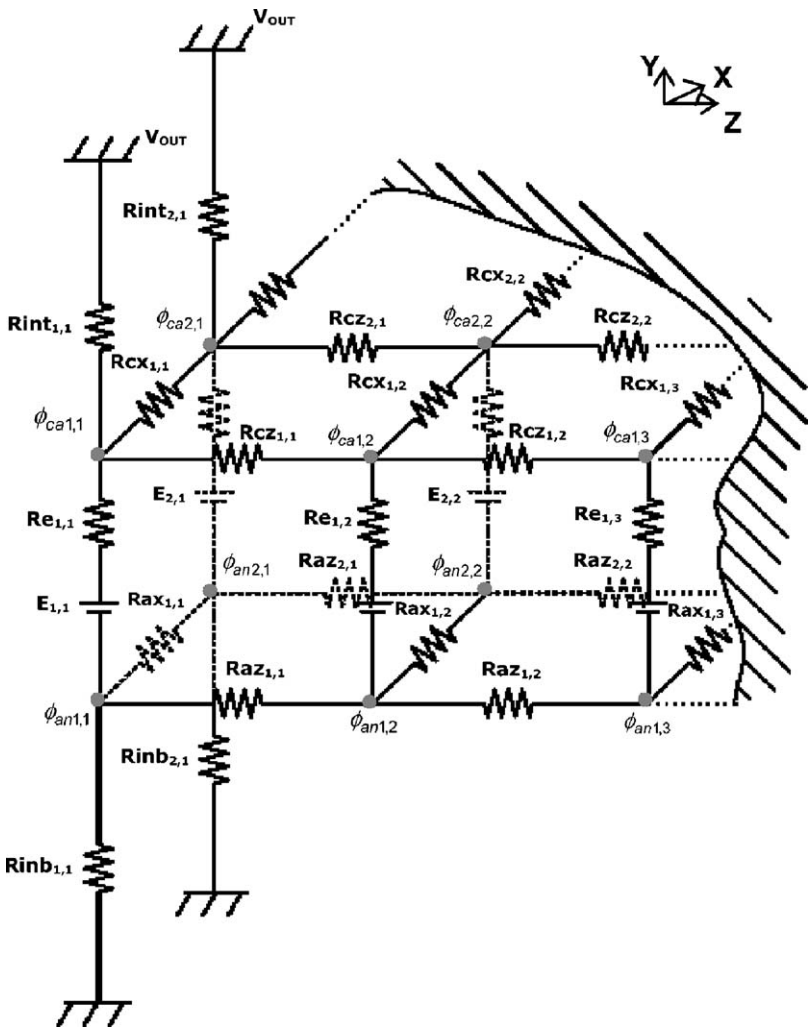

Fig. 2. Schematic of the equivalent electrical circuit.

$$\eta_{\mathrm{act,ca}} = \frac{R_\mathrm{g}T}{F}\sinh^{-1}\left(\frac{i}{2i_{0\mathrm{c}}}\right) \tag{22}$$

The concentration overpotentials at electrodes are calculated as:

$$\eta_{\mathrm{con}} = \frac{R_\mathrm{g}T}{4F}\ln\left(\frac{p_{\mathrm{O_2}}}{p^{\mathrm{r}}_{\mathrm{O_2}}}\right) \tag{23}$$

where $p_{\mathrm{O_2}}$ and $p^{\mathrm{r}}_{\mathrm{O_2}}$ are the partial pressures of oxygen at electrode/channel interface and on the reaction site, respectively. The distribution of local current density must be calculated repeatedly and the calculation must be converged to satisfy the same output voltage (V_{out}) between the upper and lower surfaces of the interconnectors. Once the electrical potential at each node is known, the local current density can be calculated as:

$$i(x,z) = \frac{E - \eta_{\mathrm{act}}(i) - \phi_{\mathrm{ca}} - \phi_{\mathrm{an}}}{R_e A_{\mathrm{area}}} \tag{24}$$

with Nernst potential:

$$E = E_0 + \frac{R_\mathrm{g}T}{2F}\ln\left(\frac{p_{\mathrm{H_2}}p^{0.5}_{\mathrm{O_2}}}{p_{\mathrm{H_2O}}}\right) \tag{25}$$

where R_{e} is the electrolyte resistance and A_{area} is the active area. ϕ_{ca} and ϕ_{an} are electrical potentials at cathode/air and anode/fuel interfaces, respectively. $p_{\mathrm{H_2}}$ and $p_{\mathrm{H_2O}}$ are partial pressures of hydrogen and water at interfaces between electrodes and electrolyte, respectively. $E_0 = 1.2723 - 2.7645 \times 10^4 T$ is a function of temperature at reaction location [18]. The thermo-fluid model and electrochemical model are coupled by the boundary conditions at interfaces:

$$-m''_{\mathrm{O_2}} = -D_{\mathrm{O_2,air}}\frac{\partial C_{\mathrm{O_2}}}{\partial y} + C_{\mathrm{O_2}}\nu_{\mathrm{int,air}} \tag{26}$$

$$m''_{\mathrm{H_2O}} = -D_{\mathrm{H_2O,fuel}}\frac{\partial C_{\mathrm{H_2O}}}{\partial y} + C_{\mathrm{H_2O}}\nu_{\mathrm{int,fuel}} \tag{27}$$

$$m''_{\mathrm{H_2O}} = -m''_{\mathrm{H_2}} \tag{28}$$

where $m''_{\mathrm{O_2}}$ and $m''_{\mathrm{H_2O}}$ are the molar production or consumption rate of oxygen and water at the cathode/electrolyte and anode/electrolyte interfaces, respectively. $\nu_{\mathrm{int,air}}$ and $\nu_{\mathrm{int,fuel}}$ are the interfacial velocities induced by local mass flux and defined

Table 1
Model input parameters for the baseline case

Parameters and conditions	Value
Fuel inlet temperature (K)	1100
Air inlet temperature (K)	1100
Inlet pressure (Pa)	1.01×10^5
Fuel inlet velocity ($m\,s^{-1}$)	0.6
Air inlet velocity ($m\,s^{-1}$)	2.5
Cell length, L (m)	0.05
Cell width, W (m)	3.2×10^{-3}
Rib width, W_r (m)	0.4×10^{-3}
Channel height, H (m)	1.0×10^{-3}
Channel width (m)	2.4×10^{-3}
Anode thickness (m)	5×10^{-5}
Cathode thickness (m)	5×10^{-5}
Electrolyte thickness (m)	150×10^{-3}
Electric resistivity of electrolyte ($\Omega\,m$)	$2.94 \times 10^{-5} \times \exp(10350/T)$
Ionic resistivity for anode ($\Omega\,m$)	$2.98 \times 10^{-5} \times \exp(-1392/T)$
Ionic resistivity for cathode ($\Omega\,m$)	$8.114 \times 10^{-5} \times \exp(500/T)$
Interconnect resistivity ($\Omega\,m$)	1×10^{-3}
Contact resistance ($\Omega\,m^2$)	1×10^{-6}
Density of electrodes/electrolyte ($kg\,m^{-3}$)	4400
Density of interconnector ($kg\,m^{-3}$)	5700
Thermal conductivity for anode/cathode ($W\,m^{-1}\,K^{-1}$)	12
Thermal conductivity for interconnector ($W\,m^{-1}\,K^{-1}$)	11
Thermal conductivity for electrolyte ($W\,m^{-1}\,K^{-1}$)	2.7
Porosity (%)	50
Tortuosity	3
Anode exchange current density ($A\,m^{-2}$)	6300
Cathode exchange current density ($A\,m^{-2}$)	3000
Permeability of the anode and cathode (m^2)	1.7×10^{-10}
Average pore radius (m)	1×10^{-6}

as:

$$\nu_{\text{int,air}} = \frac{\sum_{i=O_2,N_2} m_i''}{\rho_{\text{air}}} \tag{29a}$$

$$\nu_{\text{int,fuel}} = \frac{\sum_{i=H_2,H_2O,\text{etc.}} m_i''}{\rho_{\text{fuel}}} \tag{29b}$$

3. Input parameters and numerical scheme

The SIMPLEC method is applied to solve the discretized equations of momentum, energy, concentration and electrical potential. Air (79% N_2 and 21% O_2) is delivered to the air channel. Fuel (15.22% CO, 4.52% CO_2, 36.8% H_2, 27.3% H_2O, and 16.16% CH_4) is delivered to the fuel channel. The average current density is set to 4000 $A\,m^{-2}$. To study the geometry effects, in each computational case one geometric parameter, such as the height of channels, rib width or cell volume, is varied while keeping the other input parameters fixed.

Some input parameters for the baseline case are extracted from literature [15,24,25] and listed in Table 1. The physical properties of common materials, which are used for electrodes and electrolyte, strongly depend on temperature. Consequently, the performance of a SOFC is significantly affected by the temperature field. For instance, the resistivity of electrolyte at 1200 K could be one or two orders of magnitude smaller than that at 900 K. This temperature effect is included in the present model. Since electrolyte-supported cells are always designed to operate at over 1100 K to avoid a larger ohmic resistance in the electrolyte, the inlet fuel and air temperatures are chosen as 1100 K in the present model. The local mass transfer coefficient $h_{m,i}$ for component i, heat transfer coefficient h, and average temperature $\overline{T}$ are defined as follows:

$$h_{m,i} = \frac{m_i''}{C_{b,i} - C_{\text{int},i}} \tag{30}$$

$$h = \frac{q''}{T_b - T_{\text{int}}} \tag{31}$$

$$\overline{T} = \int_A T\,dA \tag{32}$$

where q'' is the heat flux at the interface. $C_{\text{int},i}$ and $C_{b,i}$ are the molar concentration at the interface and for the bulk flow of component i, respectively. A is the surface area.

4. Simulation results and discussion

4.1. Baseline case

Fig. 3 provides the molar fraction profiles for different gas components at an average current density of 4000 $A\,m^{-2}$. As shown in Fig. 3(a), the oxygen concentration distribution in the z-direction is highly non-uniform. The molar fraction of oxygen under the rib is lower than those in other areas. This is because oxygen cannot diffuse well underneath the interconnector. On

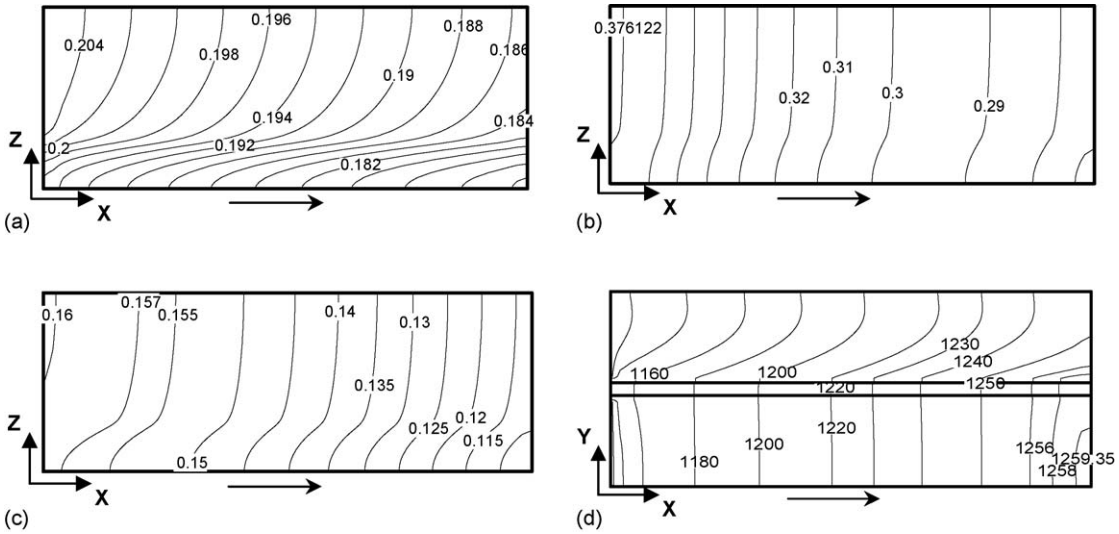

Fig. 3. Concentration contours for the baseline case: (a) oxygen at the cathode/electrolyte interface, (b) hydrogen at the anode/electrolyte interface, (c) methane at the anode/electrolyte interface, (d) temperature contour at $z = 0.001$ m (arrow denotes flow direction).

the other hand, the rib does not cause significant concentration gradients for H_2 in the z-direction since the diffusion of H_2 is about two to three times faster than those of other components as Fig. 3(b) indicates. Similarly, the molar fraction of CH_4 decreases from the fuel inlet to outlet due to the reforming reaction (Fig. 3(c)). The concentration gradients in the y-direction, which is normal to the electrolyte/anode interface, produce some concentration loss, which will be discussed later.

Fig. 3(d) shows the temperature contour on the $z = 0.001$ m plane. Along the flow direction, the temperatures increase monotonically from the inlet to the outlet due to the contribution of Joule heating and chemical reaction. For the region near the gas inlet, the temperature increases quickly and therefore causes a larger thermal stress than in other areas. On the air side, the temperature rise is not as large as that in the fuel side due to high mass fluxes. Fig. 4(a) exhibits the current density contours. It is found that the local current density profile has a peak value located roughly near the lower left corner. The local current density near the symmetric line is relatively lower because of the longest current path. In the region under the rib, the current density level is higher and their profiles are very smooth.

Fig. 4(b) shows the calculated overpotential distributions. It is found that the ohmic loss across the electrolyte and electrodes (symbol as Ele.Ohmic) represents the major source of voltage loss, followed by activation overpotentials, interconnector ohmic loss and concentration loss. The activation overpotential at the cathode and the concentration loss are relatively small. Especially, the concentration polarization is on the order of 10^{-4} (mV) and almost negligible in this case. In addition, further calculation indicates that this polarization is much higher near the rib due to a weak diffusion process. Clearly, the ohmic heating in an electrolyte contributes most to the increase in temperature. Therefore, the key elements to be focused on for improvement should be the minimization of ohmic polarization and suppressing temperature rise without significantly decreasing the cell performance. In the following sections, for the purpose of improving power density, the effects of the geometrical parameters on the SOFC performance will be analyzed.

4.2. Effects of gas flow channel dimension

Reducing the channel sizes results in a shorter current path and also facilitates higher heat/mass transport rates. This will

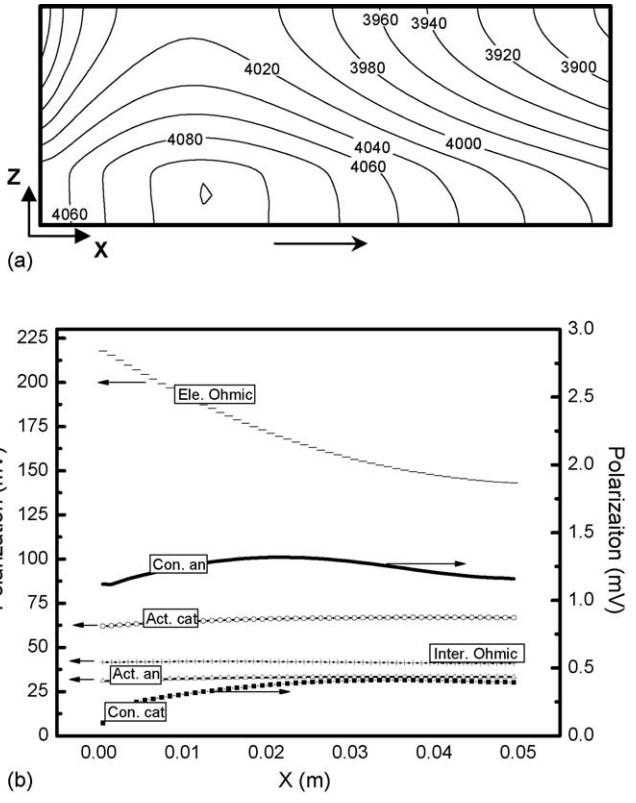

Fig. 4. Performance for the baseline case: (a) current density distribution, (b) average polarizations.

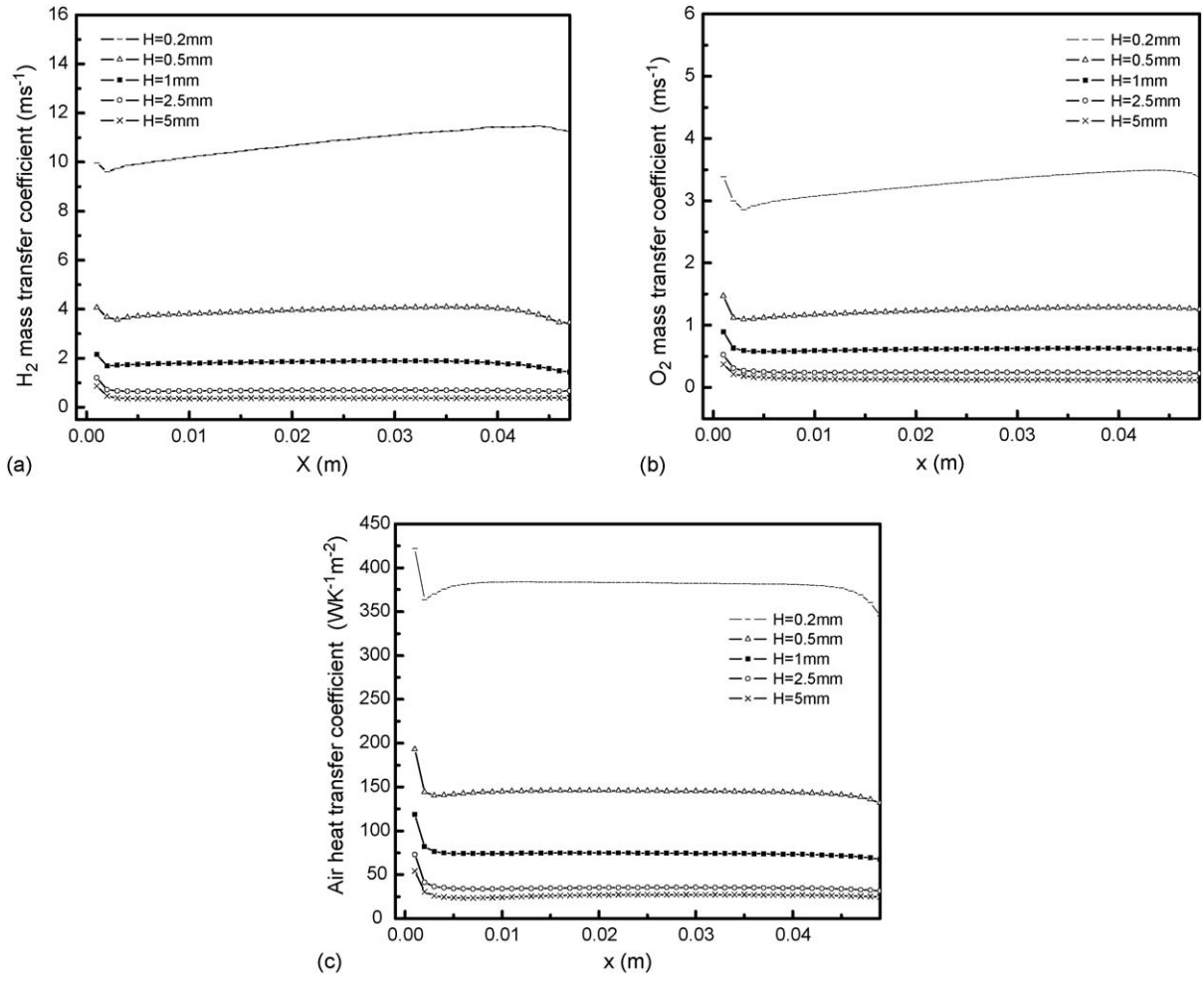

Fig. 5. Effects of the channel on the mass transfer rate (at $z = 0.001$ m plane): (a) H_2 mass transfer coefficient effect on the fuel channel, (b) O_2 mass transfer coefficient effect on the air channel, (c) heat transfer coefficient effect on the air channel.

lead to changes in temperature and concentration distributions, and the power efficiency of a SOFC.

Fig. 5(a)–(c) give the calculated mass/heat transfer coefficients on $z = 0.001$ m plane for all cases. As shown in the figure, the channels with smaller heights experience greater enhancement in the mass and heat transfer coefficients. The values of coefficients decrease sharply due to the entrance effect in the region near the channel inlets. Then, the downstream values almost stay relatively constant along the flow direction. Mass accumulation in flow channels results in a small increase in mass transfer coefficients. Moreover, the increase in heat transfer rate on the air side will help remove more heat and improve the cooling effect. We may conclude that higher mass transfer rates in smaller channels will significantly reduce the concentration polarization in channel flows and improve cell's performance.

The average temperature profiles for interconnectors of various heights are shown in Fig. 6(a). When the channel dimension is decreased, the average solid temperature level steadily decreases. However, the temperature slopes of smaller channels are much steeper than those of larger channels. This means that although the larger channels have higher temperature levels, the more gradual temperature increases will alleviate the risk of severe thermal stress and thus help ensure the structural integrity of the cell components. However, higher temperature levels put a more stringing requirement for materials and thus make fuel cells susceptible to thermo-mechanical failure. The average current density distributions for different channel sizes are shown in Fig. 6(b). It turns out that the location of the peak value for the local current density shifts towards the downstream direction of the flow as the channel dimension is decreased. Moreover, the current density profiles are flattened for larger channels.

In some of previous research works [16], the interconnectors (or ribs) were assumed to have very high electrical conductivities so that the solid resistances are neglected. However, the values of ohmic resistances in interconnectors could vary up to one order of magnitude for different materials [15]. To determine the effect of the rib resistance on the cell performance, two additional cases, in which rib resistances are modified to $R = 0.2$ and $0.02\ \Omega\,\mathrm{cm}$, were investigated. Calculations show that the distributions of current density and average solid temperature are not sensitive to the change of rib resistance. However, the terminal outputs strongly depend on the rib resistances as illustrated in Fig. 6(c). For the cell with the smallest rib resistance, $R = 0.02\ \Omega\,\mathrm{cm}$, the output increases slightly with decreasing

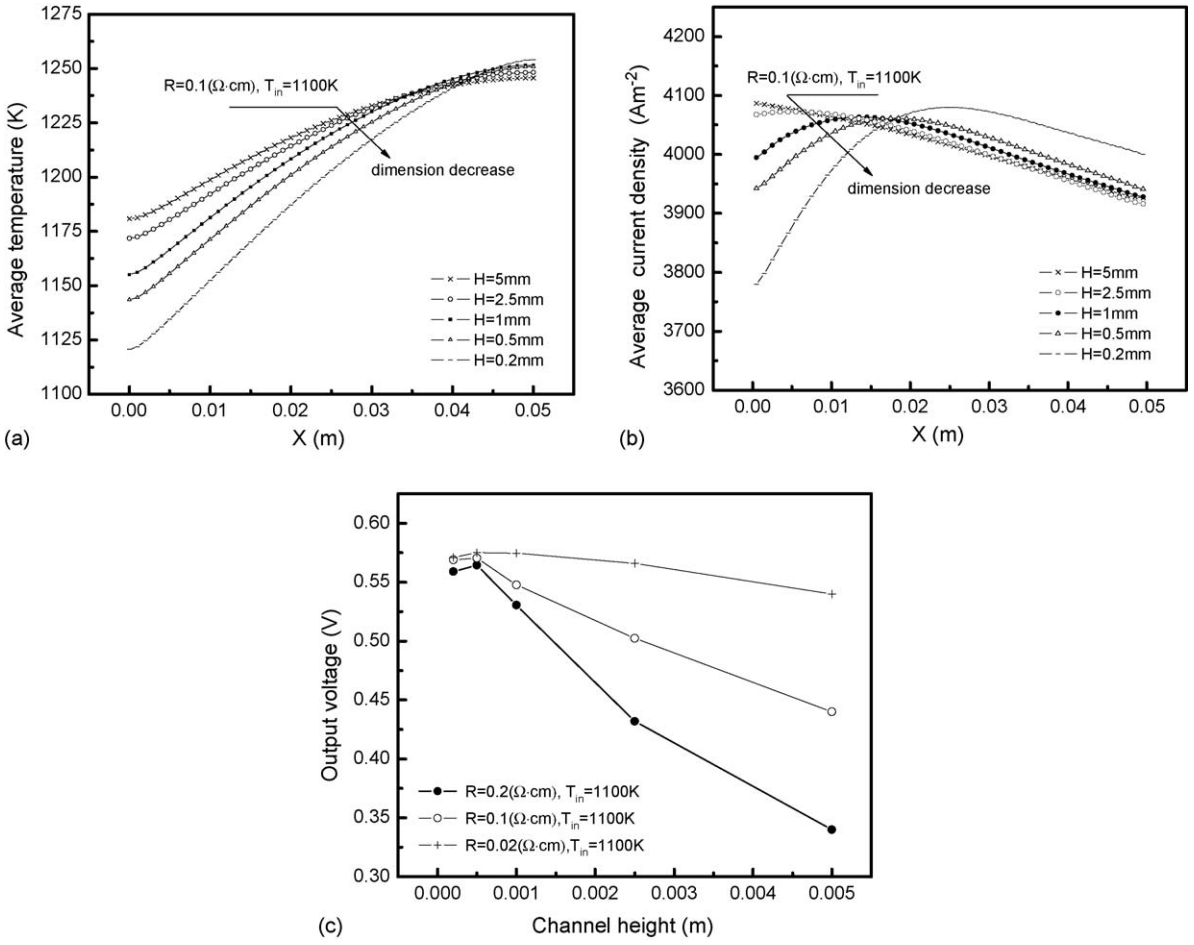

Fig. 6. Effects of the channel on cell performance: (a) average solid temperatures, (b) average current, (c) output voltage comparison.

channel dimension. As a contrast, outputs are improved remarkably with the reduction in channel dimensions for the case with higher rib resistances. It is interesting to note that the cell with the smallest channel dimension does not have the maximal terminal output. A plausible reason is that on one hand, a lower temperature increases the ohmic loss of solid part, which is a function of the operating temperature. While on the other hand, a shorter current path and a lower concentration loss may partially or totally counteract this ohmic polarization increase. In addition, an extremely small structure will lead to severe thermal stresses from a large temperature gradient. Comprehensively, the cell with the height of 0.5 mm shows the best performance in the present study.

4.3. Evaluation of thin-film electrolyte

4.3.1. Temperature effects of the baseline case

As mentioned before, the operation temperature of a SOFC needs to be maintained at a high level, which is essential to ion conductance in the electrolyte and high electrochemical reaction kinetics. However, on the other hand, higher temperatures may cause larger thermal stresses and electrode sintering [1]. As a compromise, the temperature of a SOFC is usually controlled within a reasonable range. Fig. 7(a) compares the temperature profiles and ohmic polarizations under two different inlet gas temperatures for the baseline case. Compared with a 96 K rib temperature rise in the flow direction for the case of a higher inlet gas temperature (1100 K), a larger temperature rise of 130 K was found for the case of a lower inlet gas temperature (1000 K). Therefore, it is noted that the temperature gradient in the ribs for the lower inlet gas temperature case is 30% higher, which induces more thermal stresses. The output for cell with lower inlet temperature (1000 K) decreases to 0.495 V from 0.5478 V (1100 K). In principle, lower flow temperatures retard reforming reaction speed. In addition, it is observed that the ohmic polarization is increased by over 50% due to reducing cell's temperature. From the present simulation, it is concluded that higher inlet temperature improves the efficiency of SOFC, suppresses the temperature rise and thus avoids larger thermal stress, however, with the expenses such as stringent requirements for materials and making fuel cell susceptible to thermo-mechanical failure.

4.3.2. Temperature effects of a thin-film electrolyte

One way to regain a higher fuel cell performance at a lower operating temperature is to reduce the thickness of the electrolyte. Also, the above results indicate that a smaller fuel cell can greatly reduce the concentration loss and improve the fuel cell performance. Therefore, a miniaturized SOFC with a thin-

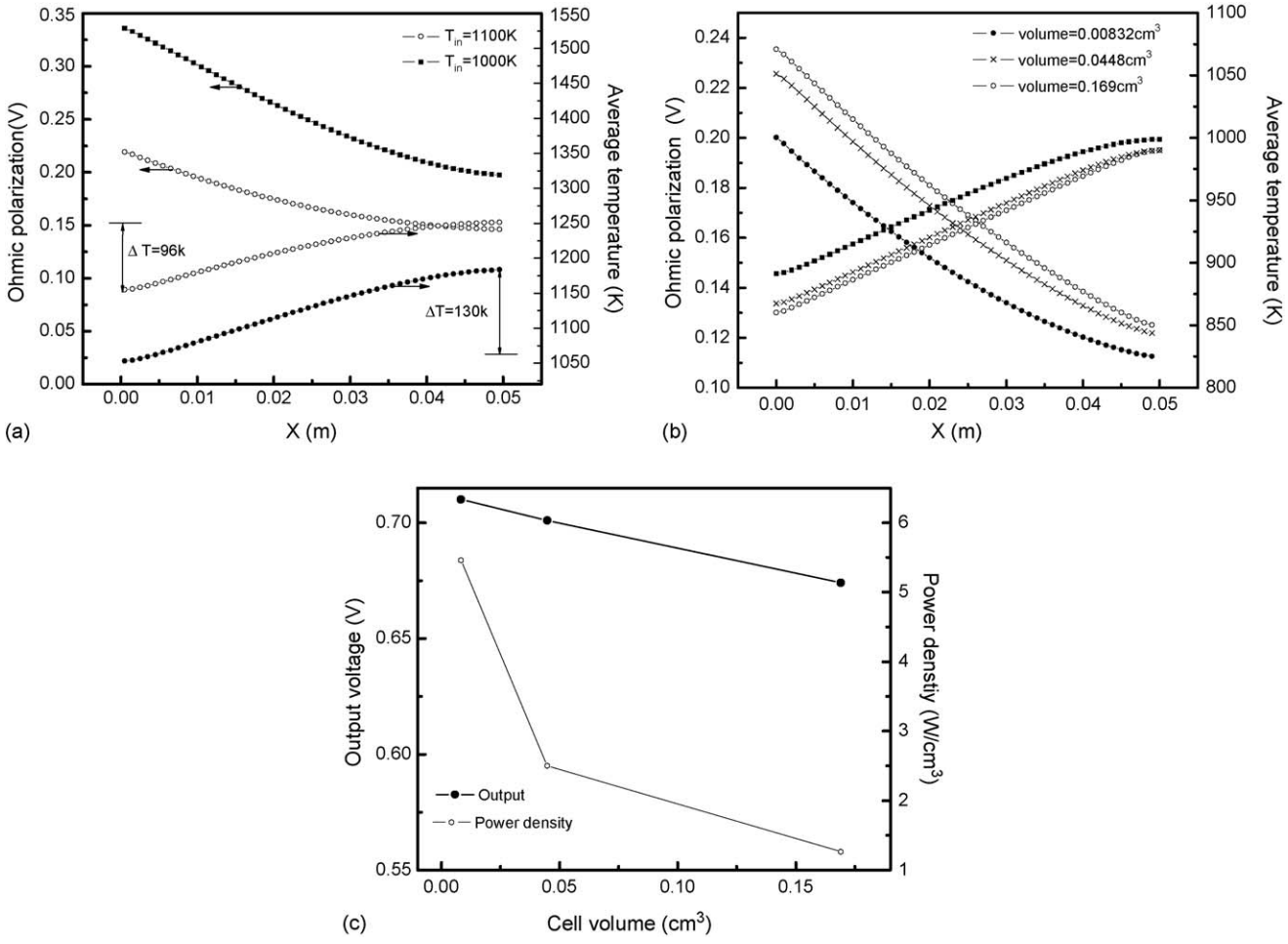

Fig. 7. Effects of temperature: (a) temperature effect on a conventional SOFC (baseline case), (b) the scaling effect on a miniaturized-thin-electrolyte SOFC with an inlet temperature of 850 K, (c) efficiency comparison.

film type electrolyte is expected to offer a better performance. In the following simulations, the thickness of electrolyte is set as 10 μm. Three different cell volumes were investigated, i.e. 0.169 cm^3 with a cross-section of $1.0 \times 3.2\,mm^2$, 0.0448 cm^3 with a cross-section of $0.5 \times 1.6\,mm^2$, and 0.00832 cm^3 with a cross-section of $0.2 \times 0.64\,mm^2$. Fig. 7(b) displays the average solid temperatures and the ohmic polarizations with a reduced inlet temperature of 850 K. The interconnector temperatures decrease with decreasing cell volumes. Compared with the results for the baseline case (Fig. 7(a)), the total temperature rises for the three cases are still at similar levels, about 105–135 K. It seems that the thermal stress levels due to temperature gradients would not be reduced for a miniaturized SOFC. For the smallest cell, the ohmic polarization is higher than those of the larger cells due to a lower operating temperature. Fig. 7(c) demonstrates a miniaturized SOFC effectively improves the output voltage and the power density. For smallest fuel cell, the power density is high, and up to 5.461 $W\,cm^{-3}$. Similar results were reported in recent work by Cha et al. [12]. They found that microchannels enhance fuel cell performance in terms of both power density and efficiency. Experimental results further revealed that the cell performance peaks for the 100 μm channels and gradually decreases with further reductions in the cell size.

4.4. Optimization of rib width

When the width of the rib is decreased for a fixed cell width, i.e. 3.2 mm, the resistances in the rib and the active reaction area will increase. At the same time, the concentration overpotential underneath the rib and the contact resistances will decrease. To achieve the maximum cell performance, the rib width should be optimized. Fig. 8(a) displays the effect of rib width on the temperature field. Clearly, a wider rib reduces the rate of temperature increase. For example, total temperature rise is suppressed by about 30 K for the widest rib (0.8 mm) as compared with the thinnest rib (0.2 mm). Thus it can be concluded that a wider rib can alleviate thermal stresses. Fig. 8(b) compares the outlet molar fractions of various gas components and the terminal output for different rib widths. Having the highest average solid temperature, the reforming and shift reactions are found to be most active in the cell with thinnest rib, consequently less H_2 and more CH_4 are consumed inside it. Moreover, Fig. 8(c) and (d) indicate that for cells with thinner ribs, the concentrations of oxygen are more uniformly distributed across the whole porous layer (z-direction), which eliminates inefficiencies that would normally be caused by obstructed "dead zones" under the ribs. Comparing with a thicker rib, the molar fraction of oxygen near

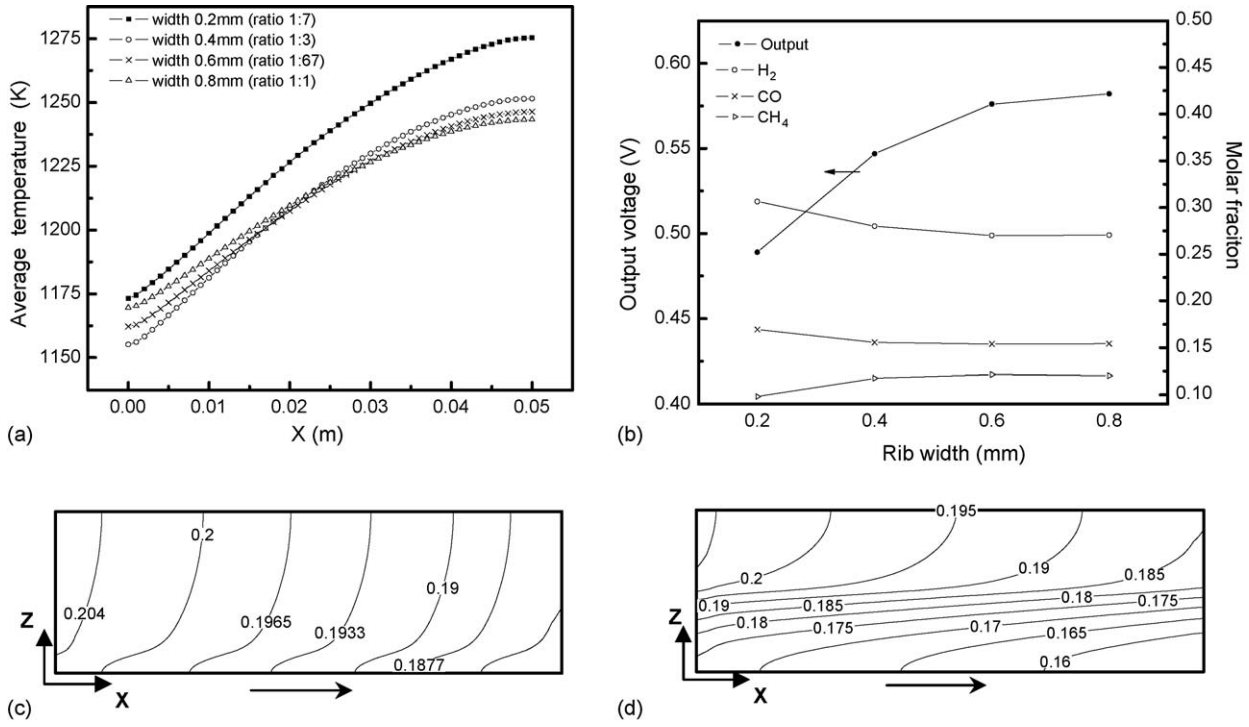

Fig. 8. Effects of rib width on the cell performance: (a) average top interconnector temperature, (b) comparison of performance, (c) oxygen at the cathode/electrolyte interface with the thinnest rib (ratio 1:7), (d) oxygen at cathode/electrolyte interface with the thickest rib (ratio 1:1).

the diffusion layer surface is significantly higher for the cell with a thinner rib. Similar tendencies are found for other reactants. However, the decrease in concentration loss for a thinner rib is not strong enough to counteract the increase in ohmic loss and thus the terminal output still decreases. So it is expected that a smaller ratio of the channel width to the rib width would serve to reduce the ohmic losses at the interface and improve cell performance.

5. Conclusions

A 3D thermo-fluid/electrochemical model was developed to evaluate the heat/mass transfer and electrochemical performance for an electrolyte-supported SOFC. Based on this model, detailed investigations were carried out to study the effects of operating temperature and geometry on the distributions of temperature, local concentration, local current density and output voltage. The main conclusions reached are listed below:

(1) When the height of flow channels is decreased, the average solid temperature is reduced accordingly and the cell efficiency is improved due to both a higher heat/mass transfer coefficient between the channel wall and flow stream and a shorter current path. However, a larger fuel cell has a more gradual temperature rise, which alleviates the risk of severe thermal stress and helps ensure the structural integrity of the cell components. If the channel height is shorter than 0.5 mm, then the cell efficiency will not be improved any further.

(2) For a conventional SOFC, if the gas inlet temperature is higher, then higher cell efficiency will result, which causes an increased cell terminal output, a lower solid temperature rise across the channel and smaller thermal stress accordingly. However, highly elevated solid temperatures usually make significant demands on materials. In comparison, the miniaturized SOFC with a thin-film electrolyte has the advantages of a lower operation temperature and an excellent performance. Conservatively, we expect that the power density of a miniaturized SOFC with a thin-film electrolyte will have the potential to exceed $10\,W\,cm^{-3}$. Of course, the average solid temperature may be relatively high and therefore, thermal management will be a challenge. However, it is noted that if the radiation loss to the environment is considered, the overall energy loss may be severe and the performance will be lowered because of a larger surface to volume ratio. In addition, the thermal-mechanical reliability of thin films should be considered in actual applications [8–10].

(3) The smaller ratio of the channel width to the rib width contributes to a reduction of the ohmic loss at the interface and thus improves the cell performance.

Overall, the present model has demonstrated that there is a trade-off among competing factors influencing the performance of a SOFC, which was not fully addressed in previous work. It should also be noted that reducing the cell volume and the electrolyte thickness and optimizing the rib width are only some of the factors influencing the performance of a SOFC. Therefore, finding better approaches or other critical parameters

to optimize the design of a SOFC will be a subject for future work.

Acknowledgements

This research was supported by the NASA Hydrogen Research for Spaceport and Space Based Applications at the University of Florida (Grant number NAG3-2930). The support by the Andrew H. Hines Jr./Progress Energy Endowment Fund is also acknowledged.

References

[1] S.C. Singhal, K. Kendall, High Temperature Solid Oxide Fuel Cells, Elsevier, New York, 2003.
[2] J. Larminie, A. Dicks, Fuel Cell Systems Explained, 3rd ed., John Wiley & Sons Inc., Chichester, West Sussex, 2003.
[3] Z. Shao, S.M. Haile, J. Ahn, P.D. Ronney, Z. Zhan, S.A. Barnett, A thermally self-sustained micro solid-oxide fuel-cell stack with high power density, Nature 435 (2005) 795–798.
[4] P.A. Ramakrishna, S. Yang, C.H. Sohn, Innovative design to improve the power density of a solid oxide fuel cell, J. Power Sources (available online at http://www.sciencedirect.com, 2005).
[5] T. Hibino, A. Hashimoto, T. Inoue, J. Tokuno, S. Yoshida, M. Sano, A low operating temperature solid oxide fuel cell in hydrocarbon–air mixtures, Sciences 288 (2000) 2031–2033.
[6] J.J. Hwang, C.K. Chen, D.Y. Lai, Detailed characteristic comparison between planar and MOLB-type SOFCs, J. Power Sources 143 (2005) 75–83.
[7] Y. Lu, L. Schaefer, Numerical study of a flat-tube high power density solid oxide fuel cell. Part II. Cell performance and stack optimization, J. Power Sources 153 (2006) 68–75.
[8] X. Chen, N.J. Wu, L. Smith, A. Ignatiev, Thin-film heterostructure solid oxide fuel cells, Appl. Phys. Lett. 84 (2004) 2700–2702.
[9] B.P. Gorman, H.U. Anderson, Processing of composite thin film solid oxide fuel cell structures, J. Am. Ceram. Soc. 88 (2005) 1747–1753.
[10] Y. Tang, K. Stanley, J. Wu, D. Ghosh, J. Zhang, Design consideration of micro thin film solid-oxide fuel cells, J. Micromech. Microeng. 15 (2005) S185–S192.
[11] P.W. Li, S.P. Chen, M.K. Chyu, Novel gas distributors and optimization for high power density in fuel cells, J. Power Sources 140 (2005) 311–318.
[12] S.W. Cha, R. O'Hayre, S.J. Lee, Y. Saito, F.B. Prinza, Geometric scale effect of flow channels on performance of fuel cells, J. Electrochem. Soc. 151 (2004) A1856–A1864.
[13] J.W. Kim, A.V. Virkar, K.Z. Fung, K. Mehta, S.C. Singhal, Polarization effects in intermediate temperature, anode-supported solid oxide fuel cells, J. Electrochem. Soc. 146 (1999) 69–78.
[14] H. Yakabe, T. Ogiwara, M. Hishinuma, I. Yasuda, 3D model calculation for planar SOFC, J. Power Sources 102 (2001) 144–154.
[15] M. Iwata, T. Hikosaka, M. Morita, T. Iwanari, K. Ito, K. Onda, Y. Esaki, Y. Sakaki, S. Nagata, Performance analysis of planar-type unit SOFC considering current and temperature distributions, Solid State Ionics 132 (2000) 297–308.
[16] P.W. Li, L. Schaefer, M.K. Chyu, A numerical model coupling the heat and gas species' transport processes in a tubular SOFC, ASME J. Heat Transfer 126 (2004) 219–229.
[17] P. Aguiar, C.S. Adjiman, N.P. Brandon, Anode-supported intermediate temperature direct internal reforming solid oxide fuel cell. I. Model-based steady-state performance, J. Power Sources 138 (2004) 120–136.
[18] S. Campanari, P. Iora, Definition and sensitivity analysis of a finite volume SOFC model for a tubular cell geometry, J. Power Sources 132 (2004) 113–126.
[19] A.V. Virkar, J. Chen, C.W. Tanner, J.W. Kim, The role of electrode microstructure on activation and concentration polarizations in solid oxide fuel cells, Solid State Ionics 131 (2000) 189–198.
[20] G. Dotelli, C.M. Mari, Modeling and simulation of the mechanical properties of YSZ/Al_2O_3 composites: a preliminary study, Solid State Ionics 148 (2002) 527–531.
[21] A.F. Mills, Mass Transfer, Prentice Hall, 2001.
[22] W. Lehnert, J. Meusinger, F. Thom, Modeling of gas transport phenomena in SOFC anodes, J. Power Sources 87 (2000) 57–63.
[23] B.A. Habeman, J.B. Young, Three-dimensional simulation of chemically reacting gas flows in the porous support structure of an integrated-planar solid oxide fuel cell, Int. Heat Mass Transfer 47 (2004) 3617–3629.
[24] S.H. Chan, K.A. Khor, Z.T. Xia, A complete polarization model of a solid oxide fuel cell and its sensitivity to the change of cell component thickness, J. Power Sources 93 (2001) 130–140.
[25] N.F. Bessette, W.J. Wefer, J. Winnick, A mathematical model of a solid oxide fuel cell, J. Electrochem. Soc. 142 (1995) 3780–3792.